Please cite this article in press as: Yang et al., Backbone rigidity encodes universal viscoelastic signatures in biomolecular condensates, Biophysical Journal (2026), https://doi.org/10.1016/j.bpj.2026.01.051

Biophysical Journal
Article

Biophysical Society

Backbone rigidity encodes universal viscoelastic signatures in biomolecular condensates

Sean Yang,[1] Subhadip Biswas,[1] and Davit A. Potoyan[1,2,*]
[1]Department of Chemistry, Iowa State University, Ames Iowa and [2]Roy J. Carver Department of Biochemistry, Biophysics, and Molecular Biology, Ames Iowa

ABSTRACT Biomolecular condensates exhibit a wide range of viscoelastic properties, shaped by their molecular grammar and composition. Coarse-grained molecular models of biomolecules are widely used to complement experiments for revealing the molecular drivers of thermodynamic stability and dynamics. However, fully flexible chain representations of proteins used in widely popular models often fail to capture their complex viscoelastic dynamics, instead predicting purely viscous responses. In this work, we demonstrate that introducing sequence-dependent chain rigidity enables us to quantitatively reproduce the experimentally observed viscelasticity trends for the low complexity domain of hnRNPA1 protein (A1-LCD) condensates and their variants. Furthermore, we show that the frequency-dependent loss factor can be characterized by a single descriptor that correlates with viscosity across A1-LCD variants and diverse parameter settings within a single-bead, semiflexible coarse-grained model. We further find that increasing backbone rigidity expands the elastic-dominated frequency range and is accompanied by more extended condensate-phase conformations. Finally, we elucidate the microscopic origins of sequence-encoded viscoelasticity by demonstrating how it can be tuned through sequence rearrangements that promote the formation of sticker clusters.

SIGNIFICANCE Using coarse-grained simulations, we demonstrate that incorporating sequence-dependent backbone rigidity into models of intrinsically disordered proteins captures key features of the experimentally observed viscoelastic behavior of condensates. Within this semiflexible coarse-grained framework for A1-LCD condensates, we identify a robust relationship between protein sequence, condensate viscosity, and elasticity, providing new insights into how sequence encodes material properties and how these can be predictively tuned.

INTRODUCTION

The phase separation of biomolecules into membraneless condensates is a ubiquitous organizing mechanism in cells for exerting spatial and temporal control over biochemical processes (1–4). The functional attributes of condensates stem from their liquid-like properties, which manifest in their ability to swiftly assemble, disassemble, fuse, and divide, allowing cells to rapidly adapt to changing environmental cues (5–8). Over time, however, condensates may lose their liquid-like material properties and age into more solid-like assemblies associated with pathological conditions (9–12). Depending on their molecular composition, condensates span a wide range of material properties: from Newtonian fluids to viscoelastic materials and gel-like states, reflecting their capacity to integrate, process, and store regulatory information at the mesoscale (13–18).

Capturing this rich spectrum of material behaviors in silico remains a significant challenge, particularly for computational models aiming to bridge molecular sequence features with mesoscopic rheology. Microrheology experiments have been instrumental in uncovering the sequence- and composition-dependent viscoelastic properties of biomolecular condensates (19–21). In addition to measuring material responses, microrheology provides access to internal dynamics and characteristic timescales associated with aging, relaxation, and flow (10,22,23). Complementing these experimental advances, sequence-resolved coarse-grained models have played a central role in elucidating the molecular origins of condensate behavior. Notably, such models have successfully reproduced key thermodynamic trends of intrinsically disordered proteins, including saturation concentrations and critical temperatures (18,24–28). A key assumption in many single-residue, sequence-resolved models is that chains are fully flexible, an approach that significantly accelerates simulations,

Submitted July 24, 2025, and accepted for publication January 28, 2026.
*Correspondence: potoyan@iastate.edu
Editor: Gregory Bowman.
https://doi.org/10.1016/j.bpj.2026.01.051

Please cite this article in press as: Yang et al., Backbone rigidity encodes universal viscoelastic signatures in biomolecular condensates, Biophysical Journal (2026), https://doi.org/10.1016/j.bpj.2026.01.051

prevents entanglement, and enables robust predictions of structural and thermodynamic properties (29). Driven by available experimental data from SAXS and turbidity measurements, most molecular models prioritize thermodynamic accuracy and structural realism over dynamic material properties, thereby overlooking the subtle role of local chain rigidity in shaping stress relaxation and energy dissipation.

Recent reports, however, (30,31) have shown that models adopting fully flexible chains fail to capture viscoelastic crossover behavior when used to calculate condensate material properties. This limitation is consistent with the well-established fact that intrinsically disordered proteins exhibit sequence-dependent chain rigidity: flexible glycine-rich segments enhance local flexibility, whereas bulky hydrophobic and aromatic residues can increase effective stiffness and lead to deviations from ideal polymer scaling (32–34). In addition, single-molecule experiments and simulation studies have revealed sequence-dependent internal friction, reflecting barriers to conformational rearrangement even in dilute solution (35–37). Although internal friction contributes to intrinsic chain reconfiguration timescales, condensates exhibit additional collective viscoelastic effects arising from intermolecular interactions, transient cross-linking, and network formation (19,31,38).

In this work, we show that introducing sequence-dependent semiflexibility into C_α coarse-grained models of A1-LCD allows us to reproduce the experimentally measured viscoelastic trends across its sequence variants (39). By designing new sequences via the reshuffling of A1-LCD residues, we also provide experimentally testable predictions for tuning the viscoelasticity of condensates through systematic variation of hydrophobic patterns. We elucidate the microscopic origins of sequence-encoded viscoelasticity by showing that rearranging residues to cluster aromatic stickers strengthens network connectivity and shifts condensates toward elastic dominance as viscosity increases. Finally, we show that appropriately rescaled spectra exhibit a collapse across the sequences and parameter perturbations studied here. This suggests that, within this model class and data set, a dominant stress-relaxation scale governs both elastic storage and viscous dissipation. Future studies should test weather adopting higher resolution models or looking at more complex protein topologies can lead to hierarchy of relaxation timescales which one may expect for heterogenuous network architectures. Nevertheless the present results establish a useful framework for engineering the material properties of condensates via sequence design, preparing the ground for rational modulation of condensate functional dynamics in cells.

MATERIALS AND METHODS

Description of models

We employed a one-bead-per-residue hydrophobicity scale (HPS) model (29) with the CALVADOS 2 parameterization (40) to simulate the low-complexity domain of protein hnRNP A1 (referred to as A1-LCD in the following text) (39). The coarse-grained (CG) beads in the chain represent the amino acid residues. The nonbonded interactions between residues i, j are modeled via the Ashbaugh-Hatch potential, and salt-screened electrostatic interactions are modeled via the Debye-Hückel potential:

$$U_{ij}^{\mathrm{AH}}(r) = \begin{cases} U^{\mathrm{LJ}}(r) - \lambda_{ij}U^{\mathrm{LJ}}(r_c) + \epsilon\left(1-\lambda_{ij}\right), & r \le 2^{1/6}\sigma_{ij} \\ \lambda_{ij}\left[U^{\mathrm{LJ}}(r) - U^{\mathrm{LJ}}(r_c)\right], & 2^{1/6}\sigma_{ij} < r \le r_c, \\ 0, & r > r_c, \end{cases} \tag{1}$$

$$U_{ij}^{\mathrm{DH}}(r) = \frac{q_i q_j e^2}{4\pi\varepsilon}\frac{\exp(-\kappa r)}{r}, \tag{2}$$

where $\epsilon = 0.8368$ kJ/mol, $r_c = 4$ nm, and U^{LJ} is the Lennard-Jones potential $U_{ij}^{\mathrm{LJ}}(r) = 4\epsilon\left[\left(\sigma_{ij}/r\right)^{12} - \left(\sigma_{ij}/r\right)^{6}\right]$. Here, $\sigma_{ij} = \left(\sigma_i + \sigma_j\right)/2$ and $\lambda_{ij} = \left(\lambda_i + \lambda_j\right)/2$ are arithmetic averages of monomer size and hydrophobicity value, respectively. The pair potential with $\lambda = 0$ consists of only the repulsive term equivalent to the Weeks-Chandler-Andersen functional form (41). We use σ values of amino acids from van der Waals volumes (42). We use λ values of amino acids from the CALVADOS 2 parameters (40). In the Debye-Hückel potential, q is the charge number of particles, and $\kappa^{-1} = \sqrt{\varepsilon k_{\mathrm{B}}T/2e^2I}$ is the Debye length, where ε is the dielectric constant, and I is the ionic strength. We take $I = 0.17$ M, $T = 300$ K, and $\kappa^{-1} = 0.9$ nm in our simulations. The temperature-dependent dielectric constant used in our simulations has the following empirical relation: $\varepsilon(T)/\varepsilon_0 = 5321/T + 233.76 - 0.9297T + 1.41710\times 10^{-3}T^2 - 8.29210\times 10^{-7}T^3$. This functional form is an empirical fit for liquid water that has been adopted in prior CG electrostatic parameterizations; we use it here for consistency with the Debye-Hückel treatment in CALVADOS-type models (40). All CG beads are connected via bonded interactions modeled by harmonic potentials.

$$U^{\mathrm{b}}(r) = \frac{k_b}{2}(r - r_0)^2, \tag{3}$$

where $k_{\mathrm{b}} = 8033$ kJ/mol/nm^2, and $r_0 = 0.38$ nm. Other parameters used in the equilibration process are listed in supporting material A.

Modulating rigidity by angular potential

We employed a harmonic "bond angle" potential between two adjacent bonds in the simulations. The angular potential of residue i (Fig. 1 *A*) is expressed as

$$U_i^{\mathrm{a}} = \frac{k}{2}(\theta_i - \theta_{0,i})^2, \tag{4}$$

where k is the angular stiffness (in units of $k_{\mathrm{B}}T$/rad^2), and $\theta_{0,i}$ is the preferred bond angle for residue i. These are adjustable parameters, and their variation is systematically explored in Table 1.

We quantify rigidity by the tangent correlation and the persistence length of a single chain. In the discrete Kratky-Porod model, the tangent correlation is $\langle(r_i - r_{i-1})(r_{i+1} - r_i)\rangle = \langle\cos\theta\rangle$, where $\langle\cos\theta\rangle$ is the average cosine of the bond angle. In our CG model, the natural bond length is a constant r_0; the corresponding discrete persistence length is $l_p = -r_0/\ln(\langle\cos\theta\rangle)$ in regimes where $\langle\cos\theta\rangle > 0$. The local rigidity of different parameter sets is shown in Fig. S2.

Please cite this article in press as: Yang et al., Backbone rigidity encodes universal viscoelastic signatures in biomolecular condensates, Biophysical Journal (2026), https://doi.org/10.1016/j.bpj.2026.01.051

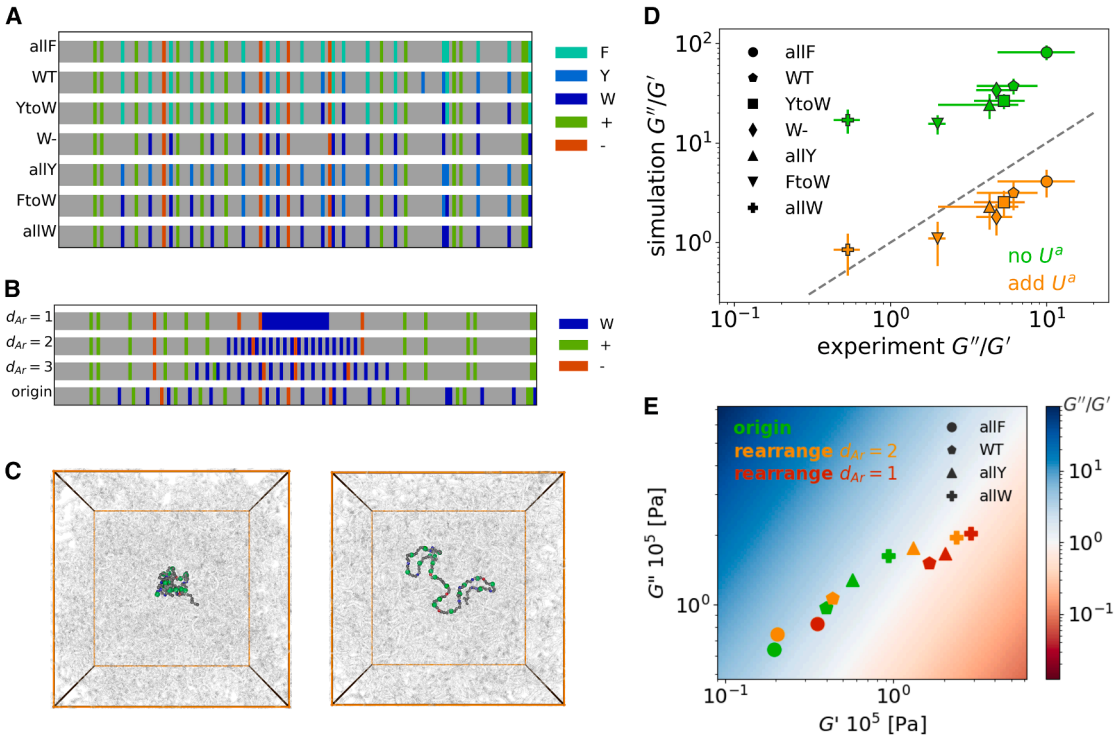

FIGURE 1 Comparison of viscous and elastic moduli between simulations and experiments. (*A* and *B*) The amino acid sequences of seven aromatic mutants of A1-LCD and their rearrangements. d_{Ar} describes the distance of the closest aromatic residues. (*C*) Representative chain conformations in condensates without and with the harmonic angular potential U^a; for visualization clarity, the transparency of the remaining condensate environment is increased. (*D*) Comparison of loss factor G''/G' between experiments (39) and simulations with (*orange*) or without (*green*) angular potential U^a . In simulations, G''/G' is taken at a characteristic frequency $\omega = 8 \times 10^{-5}$ ps^{-1} between the crossover points of allY and allW, in the same manner as in the experiment. The dashed line shows robust agreement between the experiment and the simulations. (*E*) Comparison of elastic (G') and viscous (G'') moduli at $\omega = 8 \times 10^{-5}$ ps^{-1} for different rearrangemed A1-LCD variants. The white diagonal line ($G'' = G'$) separates the dominantly viscous (*blue*) versus elastic (*red*) regimes.

Sequence rearrangement protocol and patterning metrics

We rearrange representative sequences (allF, WT, allY, and allW) with the following protocol: only aromatic residues are rearranged into the centered region of the chain with the same index distance d_{Ar} between nearest-neighbor aromatic residues (Fig. 1 *B*). The type and order of all other residues are kept the same. When $d_{\mathrm{Ar}} = 1$, all aromatic residues form a contiguous block; when $d_{\mathrm{Ar}} = 2$, aromatic residues are gapped with one other residue, which is located in their original order. The gap will widen if we increase the parameter d_{Ar}. When $d_{\mathrm{Ar}} > 2$, the effect of rearrangement is not strong because the distribution of aromatic residues is closer to a random permutation. We only compare $d_{\mathrm{Ar}} = 1$ and 2 with the original sequences in our manuscript. Because the fraction of aromatic residues is about 14% and these

TABLE 1 The parameter lists of various harmonic angular potentials U^a: Stiffness k and preferred bond angle $\theta_{0,i}$

Data set	k [k_BT/rad^2]	θ_0 [deg]	θ_{Ar} [deg]	$\theta_{\mathrm{Ar}\pm}$ [deg]
Adjust θ_0 (A1)	10	140	$\theta_{\mathrm{Ar}} = \theta_0$	$\theta_{\mathrm{Ar}\pm} = \theta_0$
Adjust θ_0 (A2)	10	150	$\theta_{\mathrm{Ar}} = \theta_0$	$\theta_{\mathrm{Ar}\pm} = \theta_0$
Adjust θ_0 (A3)	10	160	$\theta_{\mathrm{Ar}} = \theta_0$	$\theta_{\mathrm{Ar}\pm} = \theta_0$
Adjust k (B1)	0	/	/	/
Adjust k (B2)	4	160	$\theta_{\mathrm{Ar}} = \theta_0$	$\theta_{\mathrm{Ar}\pm} = \theta_0$
Adjust k (B3)	6	160	$\theta_{\mathrm{Ar}} = \theta_0$	$\theta_{\mathrm{Ar}\pm} = \theta_0$
Adjust k (B4)	10	160	$\theta_{\mathrm{Ar}} = \theta_0$	$\theta_{\mathrm{Ar}\pm} = \theta_0$
Adjust k (B5)	20	160	$\theta_{\mathrm{Ar}} = \theta_0$	$\theta_{\mathrm{Ar}\pm} = \theta_0$
Residue dependent (C1)	16	140	$\theta_{\mathrm{Ar}} = \theta_0$	$\theta_{\mathrm{Ar}\pm} = \theta_0$
Residue dependent (C2)	16	140	$\theta_{\mathrm{F}} = 145, \theta_{\mathrm{Y}} = 160, \theta_{\mathrm{W}} = 175$	$\theta_{\mathrm{Ar}\pm} = \theta_0$
Residue dependent (C3)	16	140	$\theta_{\mathrm{F}} = 145, \theta_{\mathrm{Y}} = 160, \theta_{\mathrm{W}} = 175$	$\theta_{\mathrm{Ar}+} = \theta_{\mathrm{Ar}}, \theta_{\mathrm{Ar}-} = \theta_0$
Residue dependent (C4)	16	140	$\theta_{\mathrm{F}} = 145, \theta_{\mathrm{Y}} = 160, \theta_{\mathrm{W}} = 175$	$\theta_{\mathrm{Ar}\pm} = \theta_{\mathrm{Ar}}$

The parameter sets (A1–A3) have constant k with increasing θ_0. The parameter sets (B1–B5) have constant θ_0 with increasing k. The parameter sets (C1–C4) have residue-dependent $\theta_{0,i}$, which is determined by the following order: 1) $\theta_{0,i} = \theta_{\mathrm{Ar}}$ when residue i is an aromatic amino acid (F, Y, or W); 2) $\theta_{0,i} = \max(\theta_{\mathrm{Ar}+}, \theta_{\mathrm{Ar}-})$ when residue $i \pm 1$ is aromatic; 3) $\theta_{0,i} = \theta_0$ when the previous two conditions are not met.

Please cite this article in press as: Yang et al., Backbone rigidity encodes universal viscoelastic signatures in biomolecular condensates, Biophysical Journal (2026), https://doi.org/10.1016/j.bpj.2026.01.051

residues are neutral, their rearrangement does not strongly affect overall electrostatic interactions. We quantify their charge distributions using the normalized sequence charge decoration; all values are close to 0, as shown in Fig. S1 *A*. As aromatic residues have higher hydrophobicity (see the λ values in the HPS model), clustering them along a 1D sequence will increase the hydropathy decoration metric. We also show the relation between sequence hydropathy decoration and viscoelasticity in Fig. S1.

Molecular simulations and viscoelasticity measurements

All simulations were performed using the OpenMM (v7.7) molecular dynamics library on GPU nodes. The number of chains in the simulation box was $N_{\text{pep}} = 250$. The initial length of the cubic box was set to 50 nm, well above the equilibrium size, to achieve a relatively low system density during initialization. After energy minimization, we used the *NVT* ensemble with a timestep of 0.01 ps. Next, by gradually shrinking the box dimensions, we increase the density of our system until it reaches the condensate density from previous phase-separation simulations. The parameters of this process are shown in supporting material A. Finally, we fix the box size and carry out 1×10^8-step *NVT* simulations for all subsequent measurements.

By the Green-Kubo (GK) relation, the shear stress relaxation modulus $G(t)$ can be determined by computing the autocorrelation of the off-diagonal components of the stress tensor. A more accurate expression can be obtained by taking into account the isotropic nature of the system (43,44).

$$G(t) = \frac{V}{5k_{\text{B}}T}\sum_{\alpha\beta}\left[\langle\sigma_{\alpha\beta}(0)\sigma_{\alpha\beta}(t)\rangle + \frac{1}{6}\langle N_{\alpha\beta}(0)N_{\alpha\beta}(t)\rangle\right], \tag{5}$$

where $N_{\alpha\beta} = \sigma_{\alpha\alpha} - \sigma_{\beta\beta}$ is the normal stress difference, and the summation contains $(\alpha\beta = xy,yz,xz)$. To avoid the typical noisy nature of $G(t)$ at long time scales, we fitted $G(t)$ to a series of Maxwell modes $G_{\text{M}}(t) = \Sigma_m G_m \exp(-t/\tau_m)$, which are equidistant in logarithmic time (44,45) (see Fig. S5). Then, elastic and viscous moduli $G'(\omega)$ and $G''(\omega)$ can be straightforwardly calculated by the Fourier transform of $G(t)$. The shear viscosity can be calculated by integrating the shear stress relaxation modulus over the relaxation time.

$$\eta = \int_0^{t_0} dt G(t) + \int_{t_0}^{\infty} dt G_{\text{M}}(t) \tag{6}$$

The division time t_0 is chosen so all the fast intramolecular oscillations of $G(t)$ have decayed, and the function becomes positive after t_0. We recorded the stress tensor every 20 steps for evaluating the short-time part of the integral and every 200 steps for assessing the long-time part of Eq. (6) in the *NVT* simulations.

Importantly, the Maxwell representation used here is multimode: $G(t)$ is fitted to a sum of exponentials with a logarithmically spaced relaxation spectrum, and all subsequent quantities ($G'(\omega)$, $G''(\omega)$, and η) are computed from the full fitted spectrum. The single-mode Maxwell expressions introduced later are used only as a minimal illustrative model to rationalize the emergence of rescaled master curves and are not assumed in the underlying analysis pipeline.

RESULTS

Sequence-dependent rigidity recapitulates viscoelasticity of A1-LCD and its variants

To reproduce experimentally observed trends among the A1-LCD sequence variants, allF, WT, allY, and allW (39), we introduce a residue-dependent angular potential U_i^a into the CALVADOS framework (Fig. 1 *A*). This term modulates local backbone rigidity based on amino acid identity. Aromatic residues, owing to their bulky side chains, are expected to increase adjacent bond angles and thereby stiffen the chain. To create experimentally testable predictions regarding how rigidity and spatial patterning shape condensate mechanics, we further analyzed two representative rearrangements that systematically alter the spacing or blockiness of aromatic residues via one- and two-residue gaps. Introducing this sequence-dependent angular potential has a clear structural consequence: chains become more extended within condensates (Fig. 1 *C*). Compared with simulations without the angular term, the residue-dependent rigidity suppresses local collapse and promotes expanded conformations in the dense phase. These qualitative differences form the structural basis for the rheological changes described below.

When comparing viscoelastic properties across variants, we find that the residue-dependent angular potential yields strikingly improved agreement with experiments. Experimental microrheology data for A1-LCD mutants are taken from Ref. (39), and simulation-experiment comparisons in Fig. 1 *D* follow the same loss-factor definition and characteristic-frequency protocol used in that work. Because CG dynamics do not provide a unique mapping to experimental time scales, we focus on reproducing relative ordering and spectral shape using the characteristic-frequency protocol of Ref. (39) rather than absolute values of ω. The loss factor G''/G' at the characteristic frequency $\omega = 8 \times 10^{-5}$ ps^{-1} reproduces the experimentally established ordering of mutants (Fig. 1 *D*). Both storage and loss moduli increase upon introducing residue-specific rigidity, relative to a constant angular potential, indicating that local stiffening promotes a denser and more mechanically robust intermolecular network. Differences among mutants are also magnified: the spread in G''/G' across variants increases substantially (Fig. 1 *D*), reflecting the cooperative action of aromatic type and spatial distribution in modulating viscoelasticity.

Because $G'(\omega)$ and $G''(\omega)$ are frequency dependent, we verified that the rank ordering of mutants and rearrangements is robust to the specific choice of comparison frequency. In practice, selecting ω within an intermediate-frequency window around $\omega = 8 \times 10^{-5}$ ps^{-1} yields the same qualitative ordering of the loss factor across variants (see Fig. S6 of the supporting material), indicating that the conclusions do not depend on a fine-tuned frequency choice.

We also investigate how the sequence-rearrangement protocol modulates viscoelasticity. In this protocol, we concentrate aromatic residues near the center of the chain while the order and number of all other residues remain unchanged (see materials and methods and Fig. 1 *B*). Both storage (G') and loss (G'') moduli increase after this rearrangement. Notably, G' increases more than G'', shifting the

Please cite this article in press as: Yang et al., Backbone rigidity encodes universal viscoelastic signatures in biomolecular condensates, Biophysical Journal (2026), https://doi.org/10.1016/j.bpj.2026.01.051

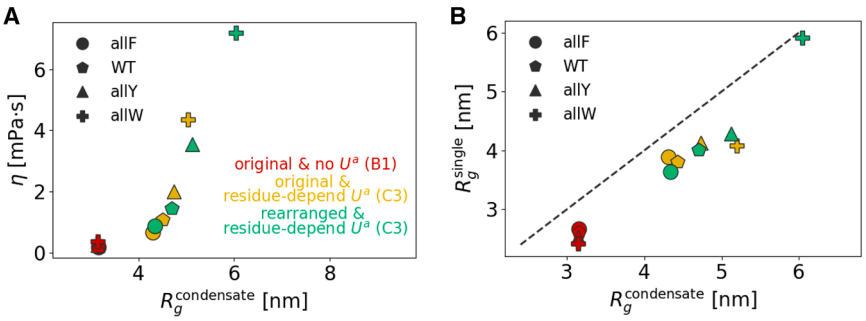

FIGURE 2 Relationship between viscosity and chain conformation. (*A*) Viscosity η as a function of radius of gyration R_g under different rigidity and connectivity conditions for four A1 mutants (allF, WT, allY, allW). Red symbols represent constant angular potential sets (B3 of Table 1). Orange symbols represent residue-dependent parameter sets (C3 of Table 1). Green symbols represent rearranged sequences ($d_{Ar} = 2$) with C3 sets. (*B*) R_g in dilute phase as a function of R_g in condensates. The dashed line shows $R_g^{condensate}/R_g^{single} = 1$.

condensates toward elastic dominance. This shift is reflected by the movement of the rearranged data points from the blue to the red region in Fig. 1 *E*. The elastic transformation induced by the enhanced connectivity of the aromatic stickers suggests experimentally testable predictions for the viscoelastic consequences of rearrangement.

At low frequencies, all sequences exhibit the expected terminal relaxation regime, with $G'(\omega) \propto \omega^2$ and $G''(\omega) \propto \omega$, leading to $G''/G' \propto \omega^{-1}$ (17). In the intermediate-frequency regime, the slower growth of $G'(\omega)$ generates a characteristic turning point in the loss factor curves (Fig. 3), marking the transition toward an increasingly elastic-dominated response. Together, these results demonstrate that aromatic identity and local concentration cooperate to enhance both viscous and elastic moduli, shifting condensates toward a more elastic regime. Having established these rheological consequences, we next examine how changes in chain dimensions quantitatively correlate with viscosity across mutants and rearrangements.

To obtain R_g^{single}, we performed independent dilute-solution simulations of a single A1-LCD chain in a cubic box at the same temperature, ionic strength, and CG force-field parameters as in the condensate simulations, but at sufficiently low concentration to eliminate interchain contacts (see supporting material B for details). Unless otherwise noted, all reported R_g values are computed directly from our simulations.

Fig. 2 quantifies these relationships among conformational properties. Across all mutants, condensate-phase chains are consistently more extended than isolated chains, with $R_g^{condensate} > R_g^{single}$ for all cases (Fig. 2 *B*). This expansion is further amplified when residue-dependent angular rigidity is included, consistent with the qualitative snapshots of Fig. 1 *C*. Increasing hydrophobicity in single-chain simulations produces modest compaction, yet condensate-phase R_g remains comparatively insensitive to aromatic identity, reinforcing the notion that intramolecular attractions dominate collapse in dilute conditions. In contrast, condensate environments, with their dense steric network and restricted configurational space, favor more extended conformations.

These changes in R_g correlate strongly with viscosity (Fig. 2 *A*). In the absence of angular rigidity (red symbols), the four mutants occupy a narrow band of viscosities. In contrast, residue-dependent angular rigidity (orange symbols) significantly separates the mutants and reproduces the experimentally observed ordering. Rearranged sequences ($d_{Ar} = 2$, green symbols) further illustrate how aromatic clustering modulates chain extension and, consequently, rheological behavior. Thus, we find that increasing local rigidity and interchain hydrophobic attraction lead to a monotonic rise in effective viscosity η, reflecting stronger network connectivity and reduced configurational mobility. This increase is consistent with classical mechanisms of viscous dissipation (38,46,47) and with our previous analysis of microscopic flow pathways. Corresponding R_g and viscosity values for almost all parameter sets are provided in Fig. S3.

Chain rigidity modulates transition between viscous and elastic regimes

To quantify the transition between viscous and elastic behavior, we extract the relaxation time τ_R from the crossover frequency at which $G'(\omega) = G''(\omega)$ (see insets in Fig. 3). If no crossover is observed, no relaxation time is assigned. We compare two cases: 1) simulations with a uniform constant angular potential ($k = 0 - 20, \theta_0 = 160°$) and 2) simulations with residue-dependent angular rigidity, which matches very closely with experimental measurements from Ref. (39). Simulations incorporating residue-dependent rigidity yield relaxation times that track experimental trends far more faithfully than constant-rigidity models, underscoring the importance of sequence-encoded stiffness in shaping condensate viscoelasticity.

We find that for weak or absent angular rigidity (flexible chain regime), condensates remain dominantly viscous: $G''(\omega) > G'(\omega)$ over the entire frequency range (Fig. 3 *A* and *B*). Increasing k stiffens local chain segments and suppresses angular flexibility, causing $G'(\omega)$ to rise more rapidly with frequency. This produces a clear viscous-to-elastic transition marked by a crossover at intermediate ω. For example, in the allW mutant, increasing k from 0 to 6 produces a crossover near 2×10^{-4} ps^{-1}, corresponding to $\tau_R \approx 4.5$ ns (Fig. 3 *C*). Further increasing rigidity ($k = 20$) shifts the crossover to lower frequencies and yields a substantially slower relaxation time ($\tau_R \approx 19$ ns), consistent with more persistent elastic stresses. We report

Please cite this article in press as: Yang et al., Backbone rigidity encodes universal viscoelastic signatures in biomolecular condensates, Biophysical Journal (2026), https://doi.org/10.1016/j.bpj.2026.01.051

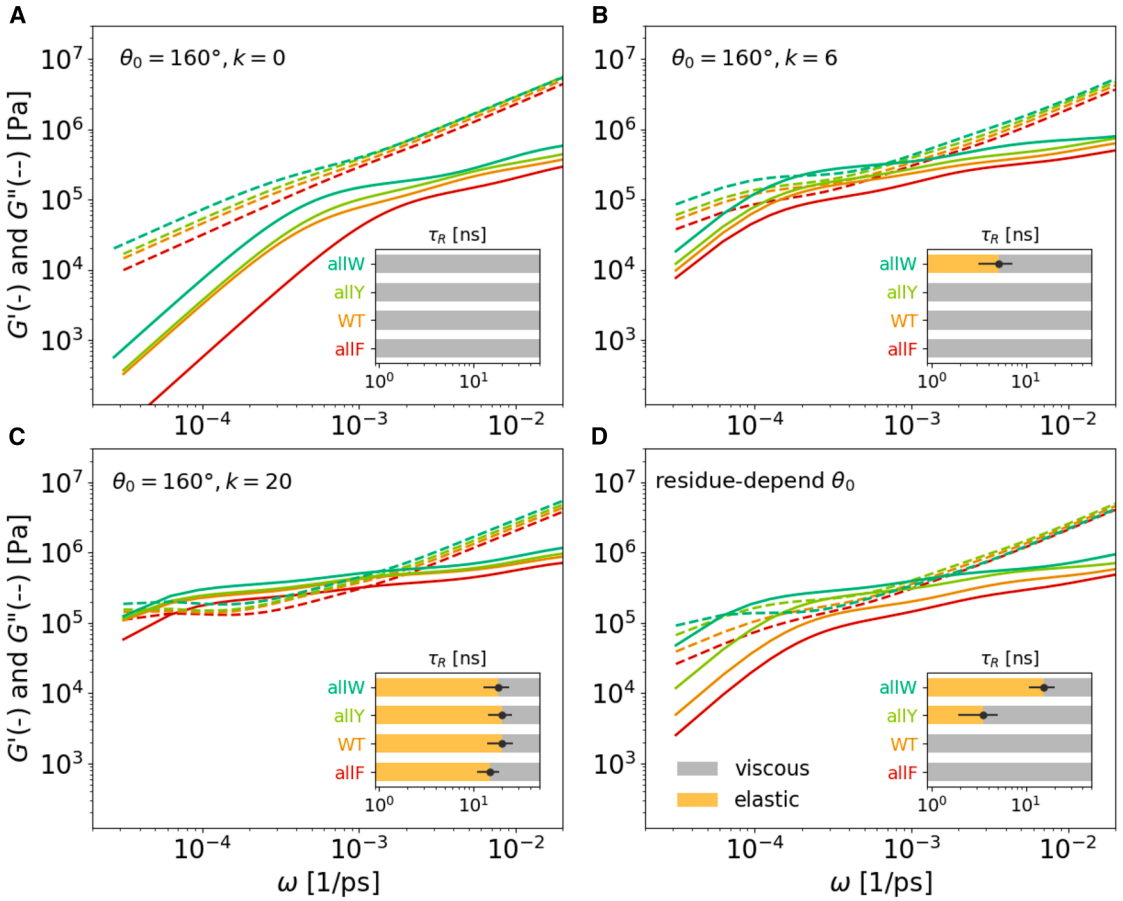

FIGURE 3 Angular potential modulates viscoelastic moduli and relaxation times. Elastic $G'(\omega)$ (*solid lines*) and viscous $G''(\omega)$ (*dashed lines*) moduli for four A1-LCD mutants under different angular potentials. (*A–C*) Constant angular potentials with rigidity k increasing from 0 to 20 (sets B1, B3, B5). (*D*) Residue-dependent angular potential (set C3). Insets show relaxation times τ_R obtained from the crossover points ($G' = G''$), separating viscous and elastic regimes.

uncertainties of G''/G' and τ_R by combining block-bootstrap GK estimates and error estimation in Maxwell fitting process. Two examples are shown in Fig. S6.

We also investigate how aromatic mutations modulate these trends. Without angular rigidity ($k = 0$), increasing hydrophobicity from allF to allW elevates both G' and G'', but G''/G' remains above 1 for all mutants, indicating a persistent viscous regime (Fig. 3 *A*). Introducing moderate rigidity ($k = 6$) induces a crossover for hydrophobic-rich sequences, but the resulting relaxation times remain significantly lower than experimental values, suggesting insufficient resistance to backbone bending. At high rigidity ($k = 20$), all mutants become elastic dominated ($G''/G' < 1$), and τ_R increases with aromatic content (Fig. 3 *C*), which overestimates the extent of the elastic regime for weaker hydrophobic sequences (e.g., allF and WT). For the residue-dependent rigidity case, hydrophobic-rich sequences (allY and allW) are distinguished by their crossover behavior and larger elastic-dominated regime, in qualitative agreement with experiments. Other modulations, e.g., variations in the bond angle θ_0, are shown in Fig. S4.

Sequence programs viscoelasticity via remodeling of sticker connectivity networks

To probe how aromatic patterning influences internal dynamics, we visualized condensates colored by the residue hydrophobicity parameter λ (Fig. 4 *A* and *C*) and computed the self part of the van Hove function $G_s(r,t)$, plotted as $4\pi r^2 G_s(r,t)$ versus r/σ (Fig. 4 *B* and *D*). In a homogeneous diffusive regime, $G_s(r,t)$ is approximately Gaussian in r, whereas pronounced non-Gaussian tails reflect dynamical heterogeneity.

For compact comparison across conditions, we fit the central part of the displacement distribution to a Gaussian form, $G_s(r,t) \propto \exp\left[-r^2/\alpha(t)\right]$, and we report the corresponding width parameter $\alpha(t)$ as a phenomenological measure of typical displacements. Across both allF and allW systems, rearrangements that promote stronger sticker clustering yield narrower central distributions and more evident deviations from Gaussian behavior at long times, consistent with an increased fraction of slowly relaxing particles. Conversely, the original sequences exhibit broader central

Please cite this article in press as: Yang et al., Backbone rigidity encodes universal viscoelastic signatures in biomolecular condensates, Biophysical Journal (2026), https://doi.org/10.1016/j.bpj.2026.01.051

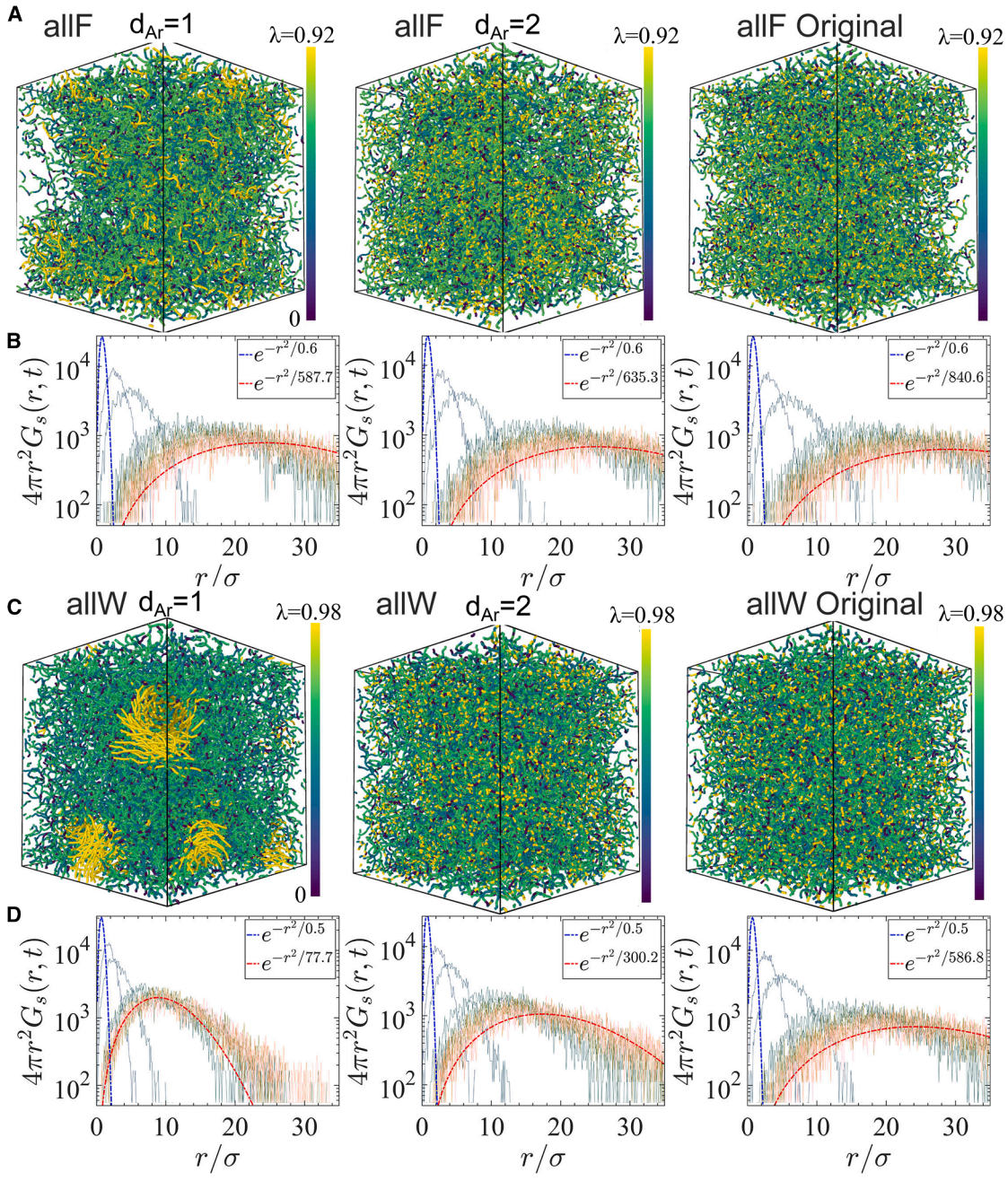

FIGURE 4 Sticker clustering analysis of A1-LCD and their rearranged sequences by varying aromatic residue clustering. (*A* and *C*) Three-dimensional visualizations of the spatial distribution of molecules colored by the hydrophobicity scale λ. Panels show the rearrangement I (*left*), rearrangement II (*center*), and original configuration (*right*), for the allF system (*A*) and allW system (*C*). (*B* and *D*) Corresponding self van Hove functions $4\pi r^2 G_s(r,t)$ plotted as a function of distance r/σ for each configuration. Curves are shown at $t = 0.5$ ps (*blue*) and $t = 1000$ ps (*red*). The Gaussian decay fit parameter, α (from $e^{-r^2/\alpha}$), is indicated in each panel.

distributions and more Gaussian-like dynamics within the same observation window.

In the most clustered condition (allW, $d_{Ar} = 1$; Fig. 4 *C*, left), high-λ residues form visually prominent sticker-rich regions, and the corresponding $G_s(r,t)$ displays the strongest suppression of forcing-scale displacements, consistent with enhanced kinetic constraints. Together, these data support the view that aromatic clustering increases dynamical heterogeneity by creating more persistent, locally connected sticker networks.

Viscoelastic quasi-universality can be seen for some sequences

Beyond variant-specific trends, our simulations reveal a quasi-universal scaling of viscoelastic response within a

Please cite this article in press as: Yang et al., Backbone rigidity encodes universal viscoelastic signatures in biomolecular condensates, Biophysical Journal (2026), https://doi.org/10.1016/j.bpj.2026.01.051

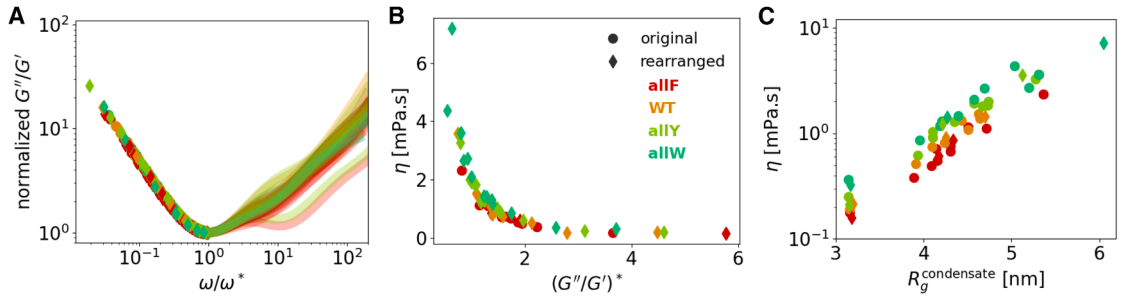

FIGURE 5 General relationship of viscoelasticity and chain conformation. All following panels contain four mutants (allF, WT, allY, allW) in their original order (*circles*) and corresponding rearranged sequences (*diamonds*); see Table S1. Four mutants of A1-LCD are represented in different colors. (*A*) Normalized loss factor G''/G' as a function of normalized frequency ω/ω^*. The low-ω part of all data follows the same curve. (*B*) Viscosity η as a function of characteristic loss factor $(G''/G')^*$. All of the data nearly collapses into a master curve. (*C*) η as a function of R_g in condensates.

single-bead semiflexible CALVADOS/HPS model. After rescaling by characteristic frequency and loss-factor minima, spectra from different sequences and angular-parameter sets collapse onto master curves, consistent with a dominant stress-relaxation timescale governing both $G'(\omega)$ and $G''(\omega)$. This behavior should be interpreted as a model-dependent prediction for single-component IDP condensates and may not persist in systems with folded domains, strong heterogeneity, or additional relaxation pathways.

We analyzed data across four categories of parameter settings: 1) variations in the preferred bond angle θ_0, 2) changes in the angular stiffness constant k, 3) introduction of residue-dependent angular potentials U_i^a, and 4) rearrangements of aromatic sequence patterns (see Table 1; Fig. 1 *B*). Despite the heterogeneity in input parameters and sequences considered, a consistent dynamic response emerges: the loss factor G''/G', which quantifies the ratio of viscous to elastic contributions and exhibits a well-defined minimum at a characteristic frequency ω^*. When normalized by this minimum value $(G''/G')^*$ and frequency ω^*, the normalized loss-factor curves superpose in the low-frequency regime (Fig. 5 *A*), revealing that each condensate's viscoelastic profile can be effectively characterized by a single descriptor, $(G''/G')^*$, which marks the point of maximal elasticity within the measured frequency window.

Strikingly, we also observe a robust inverse correlation between the shear viscosity η and $(G''/G')^*$ (Fig. 5 *B*): systems with lower $(G''/G')^*$ exhibit higher viscosities and stronger elastic dominance. A similar trend is observed in the experimental data (see Fig. S7 of the supporting material). This behavior is consistent with general principles of polymer rheology, in which longer-lived or more strongly connected networks exhibit both larger viscosities and more pronounced elastic contributions. In such systems, the dissipative and elastic responses are not independent but are coupled through the underlying relaxation spectrum and constrained by the Kramers-Kronig relations (48).

Viscosity also scales positively with the radius of gyration R_g of chains within condensates (Fig. 5 *C*). Extended conformations enhance interchain interactions and entanglements, thereby increasing viscosity. However, aromatic substitutions (e.g., F → Y → W) can increase viscosity without altering R_g, highlighting that interaction strength, beyond chain shape, plays a crucial role in viscoelastic control. The relationship between viscosity and interaction energy is shown in Fig. S8 *A*. Lastly, we show that R_g increases with the average bond angle $\langle\theta\rangle$, a proxy for local backbone rigidity (Fig. S8 *B* for $R_g^{condensate}$). Although most data follow this correlation, rearranged sequences (diamond symbols) deviate, exhibiting a greater R_g than expected, indicating that both sequence patterning and rigidity contribute independently to chain expansion and network formation.

The observed collapse of viscosity versus normalized loss factor suggests that a common relaxation timescale controls both frequency-domain viscoelastic spectra and the time-integrated stress relaxation that defines the shear viscosity. Although viscosity is often treated as a static material parameter, in equilibrium, it is determined by the time integral of the stress autocorrelation function via the GK relation (Eq. 6) and thus directly reflects the dominant stress-relaxation timescale. The dynamical behavior of associative IDP condensates can therefore be rationalized within the conceptual framework of sticky Rouse (or transient-network) models, in which reversible sticker-sticker contacts generate a dominant stress-relaxation timescale (48,49). Our central finding is that reproducing experimentally observed viscoelastic trends within a sequence-resolved CG model requires incorporating sequence-dependent effective backbone rigidity, which is not captured in standard fully flexible polymer representations. The average lifetime of reversible cross-links defines a dominant relaxation timescale, τ_R, that governs both viscous dissipation and elastic storage. In previous work, we have measured related timescales by quantifying the flow activation energies of condensates in experiments and simulations (19,38).

For intuition, this single-timescale behavior can be captured by a single-mode Maxwell model, where the

Please cite this article in press as: Yang et al., Backbone rigidity encodes universal viscoelastic signatures in biomolecular condensates, Biophysical Journal (2026), https://doi.org/10.1016/j.bpj.2026.01.051

frequency-dependent storage and loss moduli are given by the following:

$$G'(\omega) = \frac{G_0(\omega\tau_R)^2}{1 + (\omega\tau_R)^2}, \quad (7)$$

$$G''(\omega) = \frac{G_0\omega\tau_R}{1 + (\omega\tau_R)^2}. \quad (8)$$

The corresponding loss factor becomes the following:

$$\frac{G''(\omega)}{G'(\omega)} = \frac{1}{\omega\tau_R} \quad \text{for } \omega\tau_R \ll 1. \quad (9)$$

Rescaling the loss factor by its minimum value $(G''/G')^*$ and the corresponding frequency ω^* effectively factors out differences in τ_R between systems and can reveal a shared relaxation mechanism. Variations in chain rigidity or sequence composition alter the value of τ_R, but not necessarily the functional form of $G''(\omega)/G'(\omega)$ in the low-frequency regime, leading to the observed collapse onto a master curve. We note that the long-time tail of $G(t)$ is intrinsically noisy in GK calculations; therefore, inferred low-frequency moduli and η can be sensitive to the stability and functional form of the Maxwell-spectrum fit (Fig. S5). This uncertainty is mitigated by block averaging and bootstrapping (Fig. S6), but it remains a practical limitation in extracting extremely low-frequency rheology from finite-time simulations.

DISCUSSION

Biomolecular condensates exhibit tightly regulated material propertiesdysregulation of which is linked to pathological solidification in neurodegenerative diseases (10,20,50). Although molecular simulations have greatly advanced our understanding of condensate formation and thermodynamics, standard CG models that treat IDPs as fully flexible polymers fail to capture their viscoelastic response (30,31). These models typically portray condensates as predominantly viscous, whereas experimental microrheology reveals a substantial elastic component.

Here, we demonstrate that introducing sequence-dependent backbone rigidity via angular potentials enables CG simulations to recover key viscoelastic signatures observed in hnRNP A1-LCD condensates (39). Increasing local stiffness systematically expands the frequency range dominated by elasticity, shifts the viscoelastic crossover to lower frequencies, and yields relaxation times that more closely track experimental trends. These features are absent in fully flexible models. At the structural level, this stiffness manifests as an increase in the chain radius of gyration within condensates, indicating that semiflexible chains resist local collapse and adopt more extended conformations. These expanded conformations, in turn, correlate positively with condensate viscosity, linking sequence-encoded rigidity to macroscopic rheology.

Our results also highlight the importance of sequence patterning and sticker connectivity. Guided by the recently proposed energy-landscape view of condensate viscoelasticity (31), we showed that rearranging aromatic residues to enhance sticker clustering further amplifies elastic response and slows stress relaxation. Rearranged sequences reorganize the underlying sticker network, generating more pronounced structural and dynamic heterogeneity, as reflected in deviations from Gaussian behavior in the self van Hove functions. Thus, not only the overall aromatic content but also its spatial distribution along the chain play a key role in programming condensate mechanics by remodeling the connectivity and heterogeneity of sticker-mediated networks.

Within the family of A1-LCD-based sequences studied here, which share the same protein length and closely related composition but differ in charge patterning and aromatic distribution, we observe a consistent master-curve collapse of viscoelastic spectra. When the loss factor G''/G' and frequency ω are normalized by the minimum loss factor and its characteristic frequency, data from different mutants, angular potentials, and sequence rearrangements collapse onto a common curve. This behavior suggests that condensate viscoelasticity, within the single-bead semiflexible framework considered here, is governed by a shared relaxation mechanism rooted in the transient connectivity of sticker-sticker networks (19,38). In this picture, the dominant relaxation timescale is set by a combination of backbone rigidity, sticker interaction strength, and sequence patterning, which together determine both chain expansion and the lifetime of network connections. These observations indicate that some aspects of viscoelastic spectra may exhibit quasi-universal trends under restricted sequence perturbations. Future studies should clarify the conditions under which this quasi-single-timescale picture holds and when additional relaxation modes become essential.

Together, these findings establish a general framework linking sequence-encoded chain stiffness, sticker connectivity, and chain conformation to the emergent material properties of protein condensates. They also motivate new experimental tests. For example, microrheology combined with single-molecule measurements of chain dimensions in condensates could directly probe the predicted correlation between R_g, viscosity, and the minimum loss factor. More complex architectures, such as mixed folded-disordered systems or multicomponent condensates, are expected to introduce additional relaxation modes that challenge the single-timescale picture and provide a stringent test of the quasi-universality observed here. Future work that integrates optical-tweezers-based microrheology, sequence-resolved perturbations, and multiscale simulations will further refine this connection, advancing our ability to predict and program

Please cite this article in press as: Yang et al., Backbone rigidity encodes universal viscoelastic signatures in biomolecular condensates, Biophysical Journal (2026), https://doi.org/10.1016/j.bpj.2026.01.051

condensate mechanics from biomolecular sequence and composition.

DATA AND CODE AVAILABILITY

Simulation input files and analysis scripts used in this study are available on GitHub at https://github.com/PotoyanGroup/rigidity-simu-main.

ACKNOWLEDGMENTS

This work was supported by funds from the National Institute of General Medical Sciences, with grant no. R35 GM138243 awarded to D.A.P.

AUTHOR CONTRIBUTIONS

S.Y. and D.A.P. designed the research. S.Y. and S.B. carried out all simulations and analyses. S.Y. and D.A.P. wrote the manuscript.

DECLARATION OF INTERESTS

The authors declare no competing interests.

SUPPORTING MATERIAL

Supporting material can be found online at https://doi.org/10.1016/j.bpj.2026.01.051.

REFERENCES

1. Feric, M., N. Vaidya, …, C. P. Brangwynne. 2016. Coexisting liquid phases underlie nucleolar subcompartments. *Cell.* 165:1686–1697.
2. Banani, S. F., H. O. Lee, …, M. K. Rosen. 2017. Biomolecular condensates: organizers of cellular biochemistry. *Nat. Rev. Mol. Cell Biol.* 18:285–298.
3. Laflamme, G., and K. Mekhail. 2020. Biomolecular condensates as arbiters of biochemical reactions inside the nucleus. *Commun. Biol.* 3:773.
4. Donau, C., F. Späth, …, J. Boekhoven. 2020. Active coacervate droplets as a model for membraneless organelles and protocells. *Nat. Commun.* 11:5167.
5. Lyon, A. S., W. B. Peeples, and M. K. Rosen. 2021. A framework for understanding the functions of biomolecular condensates across scales. *Nat. Rev. Mol. Cell Biol.* 22:215–235.
6. Webber, M. J., and M. W. Tibbitt. 2022. Dynamic and reconfigurable materials from reversible network interactions. *Nat. Rev. Mater.* 7:541–556.
7. Spruijt, E. 2023. Open questions on liquid-liquid phase separation. *Commun. Chem.* 6:23.
8. Holehouse, A. S., and B. B. Kragelund. 2024. The molecular basis for cellular function of intrinsically disordered protein regions. *Nat. Rev. Mol. Cell Biol.* 25:187–211.
9. Mathieu, C., R. V. Pappu, and J. P. Taylor. 2020. Beyond aggregation: Pathological phase transitions in neurodegenerative disease. *Science.* 370:56–60.
10. Jawerth, L., E. Fischer-Friedrich, …, F. Jülicher. 2020. Protein condensates as aging Maxwell fluids. *Science.* 370:1317–1323.
11. Alberti, S., and A. A. Hyman. 2021. Biomolecular condensates at the nexus of cellular stress, protein aggregation disease and ageing. *Nat. Rev. Mol. Cell Biol.* 22:196–213.
12. Ripin, N., and R. Parker. 2023. Formation, function, and pathology of RNP granules. *Cell.* 186:4737–4756.
13. Khabaz, F., and R. Khare. 2014. Effect of chain architecture on the size, shape, and intrinsic viscosity of chains in polymer solutions: a molecular simulation study. *J. Chem. Phys.* 141:214904.
14. Tejedor, A. R., I. Sanchez-Burgos, …, J. R. Espinosa. 2022. Protein structural transitions critically transform the network connectivity and viscoelasticity of RNA-binding protein condensates but RNA can prevent it. *Nat. Commun.* 13:5717.
15. Ge, S., G. P. Carden, …, A. P. Sokolov. 2023. Associating Polymers in the Strong Interaction Regime: Validation of the Bond Lifetime Renormalization Model. *Macromolecules.* 56:2397–2405.
16. Shanbhag, S., and R. G. Ricarte. 2023. On the Effective Lifetime of Reversible Bonds in Transient Networks32. Macromolecular Theory Simulations.
17. Ricarte, R. G., and S. Shanbhag. 2024. A tutorial review of linear rheology for polymer chemists: basics and best practices for covalent adaptable networks. *Polym. Chem.* 15:815–846.
18. Sundaravadivelu Devarajan, D., J. Wang, …, J. Mittal. 2024. Sequence-dependent material properties of biomolecular condensates and their relation to dilute phase conformations. *Nat. Commun.* 15:1912.
19. Alshareedah, I., A. Singh, …, P. R. Banerjee. 2024. Determinants of viscoelasticity and flow activation energy in biomolecular condensates. *Sci. Adv.* 10:eadi6539.
20. Alshareedah, I., W. M. Borcherds, …, P. R. Banerjee. 2024. Sequence-specific interactions determine viscoelasticity and aging dynamics of protein condensates. *Nat. Phys.* 20:1482.
21. Boeynaems, S., A. S. Holehouse, …, A. D. Gitler. 2019. Spontaneous driving forces give rise to protein-RNA condensates with coexisting phases and complex material properties. *Proc. Natl. Acad. Sci. USA.* 116:7889–7898.
22. Tassieri, M., F. Del Giudice, …, J. M. Cooper. 2015. Microrheology with optical tweezers: measuring the relative viscosity of solutions 'at a glance'. *Sci. Rep.* 5:8831.
23. Ghosh, A., D. Kota, and H.-X. Zhou. 2021. Shear relaxation governs fusion dynamics of biomolecular condensates. *Nat. Commun.* 12:5995.
24. Jülicher, F., and C. A. Weber. 2024. Droplet physics and intracellular phase separation. *Annu. Rev. Condens. Matter Phys.* 15:237–261.
25. Farag, M., S. R. Cohen, …, R. V. Pappu. 2022. Condensates formed by prion-like low-complexity domains have small-world network structures and interfaces defined by expanded conformations. *Nat. Commun.* 13:7722.
26. Bremer, A., M. Farag, …, T. Mittag. 2022. Deciphering how naturally occurring sequence features impact the phase behaviours of disordered prion-like domains. *Nat. Chem.* 14:196–207.
27. Wang, J., D. Sundaravadivelu Devarajan, …, J. Mittal. 2024. Sequence-dependent conformational transitions of disordered proteins during condensation. *Chem. Sci.* 15:20056–20063.
28. Maristany, M. J., A. A. Gonzalez, …, J. A. Joseph. 2025. Decoding phase separation of prion-like domains through data-driven scaling laws. *eLife.* 13.
29. Dignon, G. L., W. Zheng, …, J. Mittal. 2018. Sequence determinants of protein phase behavior from a coarse-grained model. *PLoS Comput. Biol.* 14:e1005941.
30. Biswas, S., and D. A. Potoyan. 2024. Molecular drivers of aging in biomolecular condensates: Desolvation, rigidification, and sticker lifetimes. *PRX Life.* 2:023011.
31. Biswas, S., and D. A. Potoyan. 2025. Decoding biomolecular condensate dynamics: an energy landscape approach. *PLoS Comput. Biol.* 21:e1012826.
32. Hofmann, H., A. Soranno, …, B. Schuler. 2012. Polymer scaling laws of unfolded and intrinsically disordered proteins quantified with single-molecule spectroscopy. *Proc. Natl. Acad. Sci. USA.* 109:16155–16160.
33. Sawle, L., and K. Ghosh. 2015. A theoretical method to compute sequence dependent configurational properties in charged polymers and proteins. *J. Chem. Phys.* 143:085101.
34. Cheng, S., M. Cetinkaya, and F. Gräter. 2010. How sequence determines elasticity of disordered proteins. *Biophys. J.* 99:3863–3869.

35. Soranno, A., B. Buchli, …, B. Schuler. 2012. Quantifying internal friction in unfolded and intrinsically disordered proteins with single-molecule spectroscopy. *Proc. Natl. Acad. Sci. USA.* 109:17800–17806.

36. Echeverria, I., D. E. Makarov, and G. A. Papoian. 2014. Concerted dihedral rotations give rise to internal friction in unfolded proteins. *J. Am. Chem. Soc.* 136:8708–8713.

37. Chowdhury, A., D. Nettels, and B. Schuler. 2023. Interaction dynamics of intrinsically disordered proteins from single-molecule spectroscopy. *Annu. Rev. Biophys.* 52:433–462.

38. Yang, S., P. R. Banerjee, and D. A. Potoyan. 2024. Microscopic origins of flow activation energy in biomolecular condensates. *J. Phys. Chem. B.* 128:12348–12357.

39. Alshareedah, I., W. M. Borcherds, …, P. R. Banerjee. 2024. Sequence-specific interactions determine viscoelasticity and ageing dynamics of protein condensates. *Nat. Phys.* 20:1482.

40. Tesei, G., and K. Lindorff-Larsen. 2022. Improved predictions of phase behaviour of intrinsically disordered proteins by tuning the interaction range. *Open Res. Eur.* 2:94.

41. Weeks, J. D., D. Chandler, and H. C. Andersen. 1971. Role of repulsive forces in determining the equilibrium structure of simple liquids. *J. Chem. Phys.* 54:5237–5247.

42. Kim, Y. C., and G. Hummer. 2008. Coarse-grained models for simulations of multi-protein complexes. *J. Mol. Biol.* 375:1416–1433.

43. Ramírez, J., S. K. Sukumaran, …, A. E. Likhtman. 2010. Efficient on the fly calculation of time correlation functions in computer simulations. *J. Chem. Phys.* 133:154103.

44. Tejedor, A. R., R. Collepardo-Guevara, …, J. R. Espinosa. 2022. Time-dependent material properties of aging biomolecular condensates from different viscoelasticity measurements in molecular dynamics simulations. *J. Phys. Chem. B.* 127:4441–4459.

45. Zhang, Y., A. Otani, and E. J. Maginn. 2015. Reliable Viscosity Calculation from Equilibrium Molecular Dynamics Simulations: A Time Decomposition Method. *J. Chem. Theory Comput.* 11:3537–3546.

46. Rizk, F., S. Gelin, …, L. Joly. 2022. Microscopic Origins of the Viscosity of a Lennard-Jones Liquid. *Phys. Rev. Lett.* 129:074503.

47. Eyring, H. 1936. Viscosity, plasticity, and diffusion as examples of absolute reaction rates. *J. Chem. Phys.* 4:283–291.

48. Rubinstein, M., and A. N. Semenov. 2001. Dynamics of Entangled Solutions of Associating Polymers. *Macromolecules.* 34:1058–1068.

49. Galvanetto, N., M. T. Ivanović, …, B. Schuler. 2025. Material properties of biomolecular condensates emerge from nanoscale dynamics. *Proc. Natl. Acad. Sci. USA.* 122:e2424135122.

50. Emmanouilidis, L., E. Bartalucci, …, F. H.-T. Allain. 2024. A solid beta-sheet structure is formed at the surface of FUS droplets during aging. *Nat. Chem. Biol.* 20:1044–1052.